Resolved imaging of exoplanets with the solar gravitational lens

Slava G. Turyshev[1], Viktor T. Toth[2]
[1] *Jet Propulsion Laboratory, California Institute of Technology, 4800 Oak Grove Drive, Pasadena, CA 91109-0899, USA and*
[2] *Ottawa, Ontario K1N 9H5, Canada*

(Dated: April 12, 2022)

We discuss the feasibility of direct multipixel imaging of exoplanets with the solar gravitational lens (SGL) in the context of a realistic deep space mission. For this, we consider an optical telescope, placed in the image plane that forms in the strong interference region of the SGL. We consider an Earth-like exoplanet located in our immediate stellar neighborhood and model its characteristics using our own Earth. We estimate photon fluxes from such a compact, extended, resolved exoplanet. This light appears in the form of an Einstein ring around the Sun, seen through the solar corona. The solar corona background contributes a significant amount of stochastic noise and represents the main noise source for observations utilizing the SGL. We estimate the magnitude of this noise. We compute the resulting signal-no-noise ratios and related integration times that are needed to perform imaging measurements under realistic conditions. We conclude that an imaging mission is challenging but feasible, using technologies that are either already available or in active development. Under realistic conditions, megapixel imaging of Earth-like exoplanets in our galactic neighborhood requires only weeks or months of integration time, not years as previously thought.

I. INTRODUCTION

The challenges of direct imaging of exoplanets are well known. Planets are small, very distant, and not self-luminous. They appear on top of a highly contaminated light background [1, 2]. Resolved imaging of such objects would require prohibitively large telescopes or interferometric baselines. For instance, to image an Earth-like planet at the distance of 30 parsec (pc) with a diffraction-limited telescope, a telescope aperture of ~ 90 km would be required, which is not practical. Using optical interferometers for this purpose would not only involve variable interferometric baselines on the order of tens of kilometers but also telescope apertures of several tens of meters, each equipped with an external coronagraph [3] (e.g., starshade) to block out the light from the exoplanet's host star. Even with these parameters, interferometers would require integration times of hundreds of thousands to millions of years to reach a reasonable signal-to-noise ratio (SNR) of $\gtrsim 7$ to overcome the noise from exo-zodiacal light. As a result, direct resolved imaging of terrestrial exoplanets relying on conventional astronomical techniques and instruments is not feasible.

Motivated by these challenges, we considered the solar gravitational lens (SGL), which results from the gravitational bending of light rays that propagate near the Sun [4]. At optical or near-optical wavelengths, $\lambda \sim 1\,\mu$m, the SGL possesses truly impressive properties: significant light amplification ($\sim 2\times 10^{11}$) and angular resolution ($\sim 0.1\times 10^{-9}$ arcsec) [5]. Due to its impressive optical properties, the SGL presents us with the only realistic means to overcome the challenges of resolved exoplanet imaging, using only technologies that are presently available or in development [6]. The SGL offers a way to realize the age-long human dream to see alien worlds that may exist on terrestrial exoplanets in our galactic neighborhood, especially worlds that could harbor life [7].

To explore the imaging capabilities of the SGL, we extensively studied its optical properties [4, 5, 8–10]. We conducted a series of numerical investigations of exoplanet imaging with the SGL [11]. That work allowed us to identify the basic properties of a solar coronagraph [12, 13] and model image deconvolution [14, 15]. We were able to confirm the feasibility of using the SGL for imaging of faint sources such as distant exoplanets. These investigations focused only on the optical properties of the SGL and also on the light propagation through the plasma of the solar corona [16, 17], but not explicitly treating the corona brightness as a potential noise contribution.

Any use of the SGL requires observing the Einstein ring around the Sun, on the background of the solar corona. An initial analysis of the solar corona in the context of the SGL was offered in [18]. A more detailed investigation [19] identified the brightness of the solar corona as a significant source of noise that strongly affects imaging with the SGL by reducing the SNR and extending the per-pixel integration time. That study suggested that the total time needed to recover megapixel images even from a nearby exoplanet is beyond the realm of practical mission durations.

Meanwhile, we developed a comprehensive formalism to investigate the imaging of extended sources with the SGL under realistic observing conditions [9, 10]. As a part of that effort, we developed an estimate for the SNR that includes an updated solar corona model, established the imaging geometry, and considered observational scenarios [5]. We validated these results using numerical simulations, including both direct deconvolution and deconvolution using the method of Fourier quotients. Consequently, we were able to explore imaging with the SGL, taking into account factors not considered in [19] such as pixel spacing in the image plane. As a result, it became evident that under most

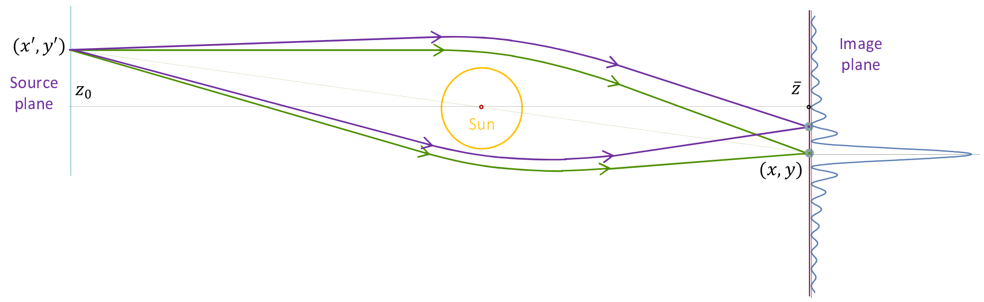

FIG. 1: The geometry of imaging a point source with the SGL. A point source with coordinates (x', y') is positioned in the source plane, at the distance z_0 from the Sun. The SGL image plane is at the heliocentric distance $\overline{z}$. Rays with different optical paths produce a diffraction pattern in the SGL image plane that is observed by an imaging telescope.

observing scenarios, high-resolution imaging of exoplanets with the SGL remains manifestly feasible with the context of a realistic near-term space mission to the focal region of the [6, 11].

Here we present a comprehensive summary of these efforts. Our objective is to evaluate the feasibility of using the SGL, establishing realistic expectations for direct multipixel imaging of exoplanets with a deep space mission that is based on available technology and executed in realistic timeframes.

Our paper is organized as follows: Section II introduces the SGL and discusses its optical properties relevant to imaging of exoplanets. In Section III we discuss the solar coronagraph that the relevant signal from the solar corona. In Section IV we calculate the signal to noise ratio and the effects of deconvolution, and compare results to numerical simulations. In Section V we discuss the results and avenues for the next phase of our investigation of the SGL.

II. SUMMARY OF THE OPTICAL PROPERTIES OF THE SGL

We consider an exoplanet as an extended source of radius $R_\oplus$, located at a large, but finite distance z_0 from the Sun, using an imaging geometry summarized in Fig. 1. The image of this object is formed in the strong interference region of the SGL, at the heliocentric position of $\overline{z} \geq R_\odot^2/2r_g$. There is no single focal point of the SGL, but a semi-infinite focal line. The SGL acts as a convex lens with negative spherical aberration. It compresses the source, forming the image of an exoplanet within the volume occupied by a cylinder with a diameter of $r_\oplus = (\overline{z}/z_0)R_\oplus \simeq 1.34 \times 10^3\,(\overline{z}/650\,\mathrm{AU})(30\,\mathrm{pc}/z_0)\,\mathrm{m}$. Placing a spacecraft in any of the image planes within the cylinder allows to take data that may be used to assemble an image of the distant, faint target.

We consider resolved imaging of extended sources with the SGL with a modest-size telescope with aperture $d \ll 2r_\oplus$ (see details in [5, 11]). The light collected by the telescope is the sum of light from the "directly imaged" region of the source and light from the rest of the planet. The directly imaged region on the source is the area with the diameter of $D = (z_0/\overline{z})d = 9.5\,(z_0/30\,\mathrm{pc})(650\,\mathrm{AU}/\overline{z})(d/1\,\mathrm{m})\,\mathrm{km}$. This directly imaged region is $2R_\oplus/D = 1340$ times smaller than the rest of the planet.

This difference between the sizes of the directly imaged region and the entire planet is important for signal estimation. As was shown in [4, 20], the point-spread function (PSF) of the SGL has the form $\propto J_0^2(k\rho\sqrt{2r_g/\overline{z}})$, where ρ is the deviation from the optical axis. For large ρ, this PSF behaves on average as $\propto 1/\rho$, which is different from the typical PSF of a thin lens that is given by $\propto (2J_1(\alpha\rho)/(\alpha\rho))^2$, which, for large ρ, behaves on average as $\propto 1/\rho^3$. The $1/\rho$ behavior of the SGL PSF implies that the telescope, although it points toward the directly imaged region, collects more light from areas far from this region. This extra signal from the rest of the exoplanet results in the emergence of blur with an intensity that may overwhelm any light received from the directly imaged region.

As the SGL PSF is know, the signal from the directly imaged region can be recovered in principle. The mapping between the source and the blurred image is linear and invertible. Deconvolution, in principle, amounts to subtracting the contribution of the blur, leaving us with only the signal of interest at each image pixel. Deconvolution can also be performed in Fourier space, leading to a significant improvement in computational efficiency, essentially making it possible to carry out deconvolution even of megapixel-resolution images without specialized computational resources, on ordinary desktop computers.

The downside of deconvolution is that it increases noise [11]. This can be understood easily in principle when we consider that deconvolution amounts to removing, from the observed signal, the contributions due to blur. However, stochastic (Gaussian or Poisson) noise by its nature is always additive. Therefore, the deconvolution process reduces the signal even as it increases noise.

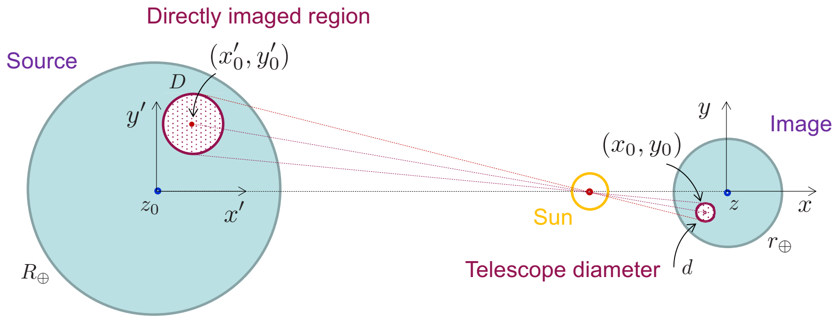

FIG. 2: Imaging of extended resolved sources with the SGL. The SGL is a convex lens, producing inverted images of a source.

Clearly, sampling frequencies – both spatial and temporal – affect the quality of the recovered image. Ultimately, image quality depends on the SNR achieved per image pixel for each position of the imaging telescope on the image plane. Our goal is to present a quantitative analysis of the resulting SNR, backed by results from computer simulations.

To describe the image of faint objects with the SGL, we take an imaging telescope and position it in the image plane at the strong interference region of the SGL. Looking back at the Sun, this imaging telescope sees an Einstein ring containing light from both the directly imaged region (contributing equally to the entire Einstein ring) and other regions of the exoplanet (contributing light to various segments of the Einstein ring). Most of the Einstein ring seen by the telescope is from light that comes from this blur, contributions from regions of the exoplanet other than the directly imaged region.

A. Signal from an exoplanet

A telescope with a modest aperture, $d \ll r_\oplus$, traversing the image plane, will receive signals from different parts of the exoplanet contributing various quantities of blur. As was shown in [5, 9], the power of the received signal at the focal plane of the imaging telescope is a function of the telescope's position on the image plane. For a uniform source brightness, the result depends only on the separation from the optical axis, ρ_0. The power received from the directly imaged region on a resolved exoplanet for $\rho = 0$ and measured along the image of the Einstein ring that forms in the focal plane of a diffraction-limited telescope is given as

$$P_{\tt fp.dir} = \epsilon_{\tt dir} B_{\tt s} \frac{\pi^2 d^3}{4\overline{z}} \sqrt{\frac{2r_g}{\overline{z}}}, \tag{1}$$

where $\epsilon_{\tt dir} = 0.77$, see [5]. The power (1) is independent of the observing wavelength and the distance to the target; however it is a strong function of the telescope's aperture, as expected.

At the same time, the power at the Einstein ring at the detector placed in the focal plane of an optical telescope is dominated by the blur and is given as

$$P_{\tt fp.blur}(\rho_0) = \epsilon_{\tt blur} B_{\tt s} \pi^2 d^2 \frac{R_\oplus}{2z_0} \sqrt{\frac{2r_g}{\overline{z}}}\, \mu(\rho_0), \qquad \text{with} \qquad \mu(r_0) = \begin{cases} \epsilon(\rho_0), & 0 \le \rho_0/r_\oplus \le 1 \\ \beta(\rho_0), & \rho_0/r_\oplus \ge 1 \end{cases}, \tag{2}$$

where $\epsilon_{\tt blur} = 0.69$ is the encircled energy fraction [5] and the factors $\epsilon(\rho_0)$ and $\beta(\rho_0)$ are given by

$$\epsilon(\rho_0) = \frac{1}{2\pi} \int_0^{2\pi} d\phi \sqrt{1 - \Big(\frac{\rho_0}{r_\oplus}\Big)^2 \sin^2\phi} = \frac{2}{\pi} {\tt E}\Big[\frac{\rho_0}{r_\oplus}\Big], \tag{3}$$

$$\beta(\rho_0) = \frac{1}{\pi} \int_{\phi_-}^{\phi_+} d\phi \sqrt{1 - \Big(\frac{\rho_0}{r_\oplus}\Big)^2 \sin^2\phi} = \frac{2}{\pi} {\tt E}\Big[\arcsin\frac{r_\oplus}{\rho_0}, \frac{\rho_0}{r_\oplus}\Big], \tag{4}$$

where ${\tt E}[x]$ is the elliptic integral and ${\tt E}[a, x]$ is the incomplete elliptic integral [21], with $\phi_\pm = \pm \arcsin(r_\oplus/\rho_0)$. The behavior of $\epsilon(\rho_0)$ and $\beta(\rho_0)$ is shown in Fig. 3. As a result, the blur's contribution in (5) is captured by factor $\mu(\rho_0)$, which, outside the directly projected image of the exoplanet, falls-off is $\propto 1/\rho_0$, as expected from the PSF of the SGL.

As a result, the total power received by the telescope is $P_{\tt exo}(\rho_0) = P_{\tt fp.dir}(\rho_0) + P_{\tt fp.blur}(\rho_0) \simeq P_{\tt fp.blur}(\rho_0)$. In other words, the total power is given by the following expression:

$$P_{\tt exo}(\rho_0) = \epsilon_{\tt blur} B_{\tt s} \pi^2 d^2 \frac{R_\oplus}{2z_0} \sqrt{\frac{2r_g}{\overline{z}}}\, \mu(\rho_0). \tag{5}$$

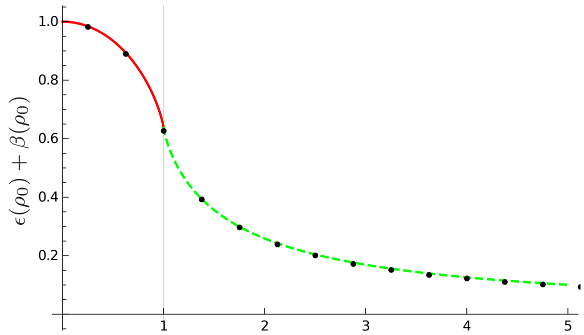

FIG. 3: Combined behavior of $\epsilon(\rho_0)$ (3), for $0 \leq \rho_0/r_\oplus \leq 1$ (in red) and $\beta(\rho_0)$ (4), for $\rho_0/r_\oplus \geq 1$ (in green). The dots represent the values obtained with a numerical simulation. (Horizontal axis is $\rho_0/r_\oplus$; similar to [9].)

Next, we express the surface brightness via familiar quantities:

$$B_s = \frac{g}{\pi}\alpha I_0, \quad [\mathrm{W/m^2sr}], \tag{6}$$

where α is the source's albedo, I_0 is the incident radiant energy emitted by the host star that is received at the top of the exoplanetary atmosphere (instellation) in units of $\mathrm{W/m^2}$. The factor g determines the surface properties of the reflector: $g = \frac{2}{3}$ for a Lambertian surface. Overall, the brightness B_s has the dimensions of $[\mathrm{W/m^2sr}]$.

TABLE I: Signal received from an exoplanet.

Parameter	Symbol	from [19]	from [5]	
Encircled energy	$\epsilon_{\tt blur}$	1	0.69	
Reflection factor	g	$\frac{1}{2}$	$\frac{2}{3}$	
Planetary albedo	α	0.3	0.3	
Solar irradiance, $[\mathrm{W/m^2}]$	I_0	1,000	1,366.83	
Telescope diameter, [m]	d	1	1	
Explanent's radius, [km]	$R_\oplus$	6,370	6,371	
Distance to exoplanet, [pc]	z_0	1.3	1.3	30
Telescope's position, [AU]	$\overline{z}$	1,200	1,200	650
Blur envelope factor	$\mu(\rho_0)$	1	$\mu(\rho_0)$	
Power received, [W]	$P_{\tt exo}(\rho_0)$	2.14×10^{-13}	2.70×10^{-13}	1.59×10^{-14}
Photon flux received, [phot/s]	$Q_{\tt exo}(\rho_0)$	1.08×10^6	1.36×10^6	8.01×10^4

Using (6) in (5), we have the following expressions for the power and photon flux received by the telescope

$$P_{\tt exo}(\rho_0) = \epsilon_{\tt blur}\, g\alpha I_0 \pi d^2 \frac{R_\oplus}{2z_0}\sqrt{\frac{2r_g}{\overline{z}}}\,\mu(\rho_0), \qquad Q_{\tt exo}(\rho_0) = \frac{\lambda}{hc}P_{\tt exo}(\rho_0). \tag{7}$$

As a general trend, Eq. (7) allows us to compute the signals as

$$\begin{aligned} P_{\tt exo}(\rho_0) &= \epsilon_{\tt blur} g\alpha I_0 \pi d^2 \frac{R_\oplus}{2z_0}\sqrt{\frac{2r_g}{\overline{z}}}\mu(\rho_0) = \\ &= 1.59 \times 10^{-14}\mu(\rho_0)\Big(\frac{\epsilon_{\tt blur}}{0.69}\Big)\Big(\frac{g}{2/3}\Big)\Big(\frac{I_0}{1366.83}\Big)\Big(\frac{d}{1\,\mathrm{m}}\Big)^2\Big(\frac{650\,\mathrm{AU}}{\overline{z}}\Big)^{\frac{1}{2}}\Big(\frac{30\,\mathrm{pc}}{z_0}\Big)\ \mathrm{W}, \end{aligned} \tag{8}$$

$$\begin{aligned} Q_{\tt exo}(\rho_0) &= \frac{\lambda}{hc}P_{\tt exo}(\rho_0) = \\ &= 8.01 \times 10^4\mu(\rho_0)\Big(\frac{\epsilon_{\tt blur}}{0.69}\Big)\Big(\frac{g}{2/3}\Big)\Big(\frac{I_0}{1366.83}\Big)\Big(\frac{d}{1\,\mathrm{m}}\Big)^2\Big(\frac{650\,\mathrm{AU}}{\overline{z}}\Big)^{\frac{1}{2}}\Big(\frac{30\,\mathrm{pc}}{z_0}\Big)\Big(\frac{\lambda}{1\,\mu\mathrm{m}}\Big)\ \mathrm{photons/s}. \end{aligned} \tag{9}$$

Although derived using a different approach (see details in [5]), the result (7), is formally identical to that published in [19]. Table I compares numerical estimates for an exoplanet located at 1.3 pc and observed through the SGL using a 1-m telescope at 1200 AU. The estimated signal levels are comparable in magnitude, with any differences due to the estimated values of $\epsilon_{\tt blur}$, g and I_0. For comparison, a third case (exoplanet at 30 pc, telescope at 650 AU) is also shown.

III. SOLAR CORONAGRAPH AND SIGNAL FROM THE SOLAR CORONA

A. Solar coronagraph

Solar coronagraphy, invented by Bernard Lyot [22], is used to study the solar corona. The idea was to reproduce solar eclipses artificially. The same idea was used to develop the concept for the SGL coronagraph.

The SGL coronagraph is different from those developed for conventional exoplanatory imaging. In those cases, the objective is to block out light from the host star, a point source. In contrast, a coronagraph for the SGL must work in the tradition of Lyot's original coronagraph, as it is needed to block light from the Sun, while allowing light in from the Einstein ring that appears on the background of the solar corona, barely separated from the solar disk.

The already available design for the SGL coronagraph [13] rejects solar light with a contrast ratio of $\sim 10^{-7}$, which is sufficient for our purposes. At this level of rejection, the light from the solar disk is reduced to the level comparable to the brightness of the solar corona. We consider two possible concepts for the coronagraph occulter. In a conventional design, which we call the "disk coronagraph", the device blocks light from the solar disk, possibly extending all the way to the inner boundary of the $1.22\lambda/d$ annulus that corresponds to the Einstein ring. In contrast, an "annular coronagraph" (Fig. 4) also blocks light outside the Einstein-ring.

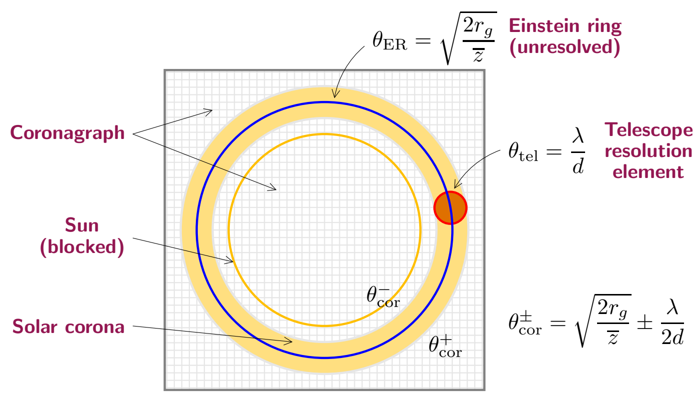

FIG. 4: The annular coronagraph concept. The coronagraph blocks light from both within and outside the Einstein ring. The thickness of the exposed area is determined by the diffraction limit of the optical telescope at its typical observational wavelength.

Compared to the disk coronagraph, the annular concept reduces the contribution of corona noise to the overall corona signal in the focal plane of the optical telescope by a factor of ~ 5. Any such reduction directly translates into a reduction of stochastic noise and a consequent decrease in the required integration time to achieve a desired SNR. Although operating an annular coronagraph aboard a spacecraft may present some challenges, those are not unsurmountable. Therefore, we assume that we will be able to rely on an annular type coronagraph implementation to help us block unwanted light from the Sun and to reduce stochastic noise due the solar corona.

B. Signal from the solar corona

As we established, the Einstein ring that forms around the Sun from light emitted by the exoplanet that is the observational target appears on the bright background of the solar corona. Even if we assume that the corona background can be accurately estimated (or measured by other instruments) and removed, as light is quantized into photons, inevitably, there is stochastic noise in the form of Poisson (approximately Gaussian) shot noise.

To estimate this noise contribution by the corona, we need to estimate the signal from the solar corona within the annulus that corresponds to the Einstein ring around the Sun, formed by light from the target exoplanet. In the region occupied by the image of the Einstein ring in the focal plane of a diffraction-limited telescope, the corona contribution is given for the two coronagraph concepts as:

$$P^{\tt disk}_{\tt cor} \;=\; \epsilon_{\tt cor}\,\pi(\tfrac{1}{2}d)^2\int_0^{2\pi}d\phi\int_{\theta_0}^{\infty}\theta d\theta\, B_{\tt cor}(\theta), \qquad\qquad P^{\tt annul}_{\tt cor} = \epsilon_{\tt cor}\,\pi(\tfrac{1}{2}d)^2\int_0^{2\pi}d\phi\int_{\theta^-_{\tt cor}}^{\theta^+_{\tt cor}}\theta d\theta\, B_{\tt cor}(\theta), \tag{10}$$

where $\theta = \rho/\overline{z}$ and $\theta_0 = R_\odot/\overline{z}$. The upper integration limit for the disk coronagraph may be reduced from ∞ to, e.g., $2\theta_0$ with only a marginal impact on the result.

For an annular coronagraph, the integration limits are given by

$$\theta^{\pm}_{\tt cor} = \sqrt{\frac{2r_g}{\overline{z}}} \pm \frac{\lambda}{2d}. \tag{11}$$

We consider both of these coronagraph concepts to describe the noise contribution from the solar corona to the imaging and spectroscopy with the SGL.

The surface brightness of the solar corona $B_{\tt cor}(\theta)$ is taken from [23]:

$$B_{\tt cor}(\theta) = 20.09\Big[3.670\Big(\frac{\theta_0}{\theta}\Big)^{18} + 1.939\Big(\frac{\theta_0}{\theta}\Big)^{7.8} + 5.51\times 10^{-2}\Big(\frac{\theta_0}{\theta}\Big)^{2.5}\Big] \ \frac{\rm W}{\rm m^2\, sr}. \tag{12}$$

Another model, the Baumbach model [24, 25], was used, e.g., in Ref. [19]:

$$B_{\tt cor}(\theta) = 18.9\Big[2.565\Big(\frac{\theta_0}{\theta}\Big)^{17} + 1.425\Big(\frac{\theta_0}{\theta}\Big)^{7} + 5.32\times 10^{-2}\Big(\frac{\theta_0}{\theta}\Big)^{2.5}\Big] \ \frac{\rm W}{\rm m^2\, sr}. \tag{13}$$

Using the disk coronagraph in conjunction with the Baumbach model, with $\theta^{+}_{\tt cor} = 2R_\odot/\overline{z}$, as it was done in [19], yields the following estimate for the photometric signal received from the solar corona:

$$P^{\tt disk}_{\tt cor} = \epsilon_{\tt cor} \times 6.78\times 10^{-10}\Big(\frac{d}{1\,{\rm m}}\Big)^2\Big(\frac{1200\,{\rm AU}}{\overline{z}}\Big)^2 \ {\rm W}, \tag{14}$$

$$Q^{\tt disk}_{\tt cor} = \epsilon_{\tt cor}\frac{\lambda}{hc}P^{\tt phot}_{\tt cor} = \epsilon_{\tt cor} \times 3.41\times 10^{9}\Big(\frac{d}{1\,{\rm m}}\Big)^2\Big(\frac{1200\,{\rm AU}}{\overline{z}}\Big)^2 \ {\rm photon/s}. \tag{15}$$

This estimate was obtained using an upper integration limit of $2\theta_0$ in (10). If we extend this integration limit to infinity, we obtain the result is slightly larger, namely $P^{\tt disk}_{\tt cor} = \epsilon_{\tt cor} \times 7.98\times 10^{-10}\big(1200{\rm AU}/\overline{z}\big)^2$ W and $Q^{\tt disk}_{\tt cor} = \epsilon_{\tt cor} \times 4.02\times 10^{9}\big(1200{\rm AU}/\overline{z}\big)^2$ photon/s.

Using the value of $\epsilon_{\tt cor} = f = 0.35$, borrowed from [19], we estimate the relevant signal on the imaging detector measured at the focal plane of the imaging telescope:

$$P_{\tt cor} = fP^{\tt disk}_{\tt cor} = 2.37\times 10^{-10}\Big(\frac{d}{1\,{\rm m}}\Big)^2\Big(\frac{1200\,{\rm AU}}{\overline{z}}\Big)^2 \ {\rm W}, \tag{16}$$

$$Q_{\tt cor} = fQ^{\tt disk}_{\tt cor} = 1.20\times 10^{9}\Big(\frac{d}{1\,{\rm m}}\Big)^2\Big(\frac{1200\,{\rm AU}}{\overline{z}}\Big)^2 \ {\rm photon/s}. \tag{17}$$

For the annular coronagraph concept, in turn, we obtained $\epsilon_{\tt cor} = 0.60$ as the fraction of the encircled energy for the solar corona [5]. Using this value, we estimated the contribution from the solar corona by integrating (12) over the observed width and circumference of the Einstein ring annulus:

$$\begin{aligned} P_{\tt cor} &= 19.48\,\epsilon_{\tt cor}\pi^2\lambda d\,\frac{R_\odot}{\overline{z}}\Big(\frac{R_\odot}{\sqrt{2r_g\overline{z}}}\Big)^{6.8}\Big[1 + 1.89\Big(\frac{R_\odot}{\sqrt{2r_g\overline{z}}}\Big)^{10.2} + 0.0284\Big(\frac{\sqrt{2r_g\overline{z}}}{R_\odot}\Big)^{5.3}\Big] = \\ &= 4.56\times 10^{-10}\Big[1 + 0.79\Big(\frac{650\,{\rm AU}}{\overline{z}}\Big)^{5.1} + 0.05\Big(\frac{\overline{z}}{650\,{\rm AU}}\Big)^{2.65}\Big]\Big(\frac{d}{1\,{\rm m}}\Big)\Big(\frac{650\,{\rm AU}}{\overline{z}}\Big)^{4.4}\Big(\frac{\lambda}{1\,\mu{\rm m}}\Big) \ {\rm W}. \end{aligned} \tag{18}$$

This corresponds to the corona photon flux of

$$Q_{\tt cor} = 2.29\times 10^{9}\Big[1 + 0.79\Big(\frac{650\,{\rm AU}}{\overline{z}}\Big)^{5.1} + 0.05\Big(\frac{\overline{z}}{650\,{\rm AU}}\Big)^{2.65}\Big]\Big(\frac{d}{1\,{\rm m}}\Big)\Big(\frac{650\,{\rm AU}}{\overline{z}}\Big)^{4.4}\Big(\frac{\lambda}{1\,\mu{\rm m}}\Big)^2 \ {\rm photons/s}. \tag{19}$$

Table II summarizes these coronal flux estimates.

IV. SIGNAL TO NOISE RATIO IN THE PRESENCE OF THE CORONA

A. Signal to noise ratio of the observed image

Assuming that the contribution of the solar corona is removable (e.g., by observing the corona from a slightly different vantage point) and only stochastic (shot) noise remains, we estimate the resulting signal-to-noise ratio as

$${\rm SNR}_{\tt C} = \frac{Q_{\tt exo}}{\sqrt{Q_{\tt exo} + Q_{\tt cor}}}, \tag{20}$$

TABLE II: Signal received from the solar corona.

Parameter	Symbol	from [19]	from [5]	
Encircled energy	f, $\epsilon_{\mathtt{cor}}$	$f = 0.35$	$\epsilon_{\mathtt{cor}} = 0.60$	
Solar corona model	$B_{\mathtt{cor}}(\rho)$	Eq. (13)	Eq. (12)	
Coronagraph width	$\Delta\theta$	$\dfrac{R_\odot}{\overline{z}} \leq \theta \leq \dfrac{2R_\odot}{\overline{z}}$	$\sqrt{\dfrac{2r_g}{\overline{z}}} - \dfrac{\lambda}{2d} \leq \theta \leq \sqrt{\dfrac{2r_g}{\overline{z}}} + \dfrac{\lambda}{2d}$	
Telescope diameter, [m]	d	1	1	
Telescope's position, [AU]	$\overline{z}$	1,200	1,200	650
Power received, [W]	$P_{\mathtt{cor}}(\rho_0)$	2.37×10^{-10}	3.96×10^{-11}	8.39×10^{-10}
Photon flux received, [phot/s]	$Q_{\mathtt{cor}}(\rho_0)$	1.20×10^{9}	1.99×10^{8}	4.22×10^{9}

in the regime dominated by the solar corona. The subscript $\mathtt{C}$ signifies that it is a signal that has been convolved by the SGL's PSF.

Using values consistent with Ref. [19] (see Table I) in the expressions for the signal from the exoplanet and the solar corona, (9) and (17), for $\overline{z} = 1200$ AU we obtain

$$Q_{\mathtt{exo}} = 1.08 \times 10^6 \Big(\frac{d}{1\,\mathrm{m}}\Big)^2 \Big(\frac{1200\,\mathrm{AU}}{\overline{z}}\Big)^{\frac{1}{2}} \Big(\frac{1.3\,\mathrm{pc}}{z_0}\Big) \Big(\frac{\lambda}{1\,\mu\mathrm{m}}\Big)\ \text{photon/s}, \tag{21}$$

$$Q_{\mathtt{cor}} = 1.20 \times 10^9 \Big(\frac{d}{1\,\mathrm{m}}\Big)^2 \Big(\frac{1200\,\mathrm{AU}}{\overline{z}}\Big)^2\ \text{photon/s}, \tag{22}$$

resulting in the following $\mathrm{SNR}_{\mathtt{C}}$ of the convolved image:

$$\mathrm{SNR}_{\mathtt{C}} = 31.16 \Big(\frac{d}{1\,\mathrm{m}}\Big) \Big(\frac{1.3\,\mathrm{pc}}{z_0}\Big) \Big(\frac{\overline{z}}{1200\,\mathrm{AU}}\Big)^{0.5} \Big(\frac{\lambda}{1\,\mu\mathrm{m}}\Big) \sqrt{\frac{t}{1\,\mathrm{s}}}. \tag{23}$$

In [5], this SNR was estimated by assuming slightly different values in (9) (see table I) along with an annular coronagraph (19):

$$Q_{\mathtt{exo}}(\rho_0) = 1.36 \times 10^6 \mu(\rho_0) \Big(\frac{d}{1\,\mathrm{m}}\Big)^2 \Big(\frac{1200\,\mathrm{AU}}{\overline{z}}\Big)^{\frac{1}{2}} \Big(\frac{1.3\,\mathrm{pc}}{z_0}\Big) \Big(\frac{\lambda}{1\,\mu\mathrm{m}}\Big)\ \text{photon/s}. \tag{24}$$

$$Q_{\mathtt{cor}}(\rho_0) = 1.54 \times 10^8 \Big[1 + 0.04 \Big(\frac{1200\,\mathrm{AU}}{\overline{z}}\Big)^{5.1} + 0.25 \Big(\frac{\overline{z}}{1200\,\mathrm{AU}}\Big)^{2.65}\Big] \Big(\frac{d}{1\,\mathrm{m}}\Big) \Big(\frac{1200\,\mathrm{AU}}{\overline{z}}\Big)^{4.4} \Big(\frac{\lambda}{1\,\mu\mathrm{m}}\Big)^2\ \text{photons/s}, \tag{25}$$

which results in the following SNR of the convolved image:

$$\mathrm{SNR}_{\mathtt{C}}(\rho_0) = \frac{109.11\,\mu(\rho_0)}{\sqrt{1 + 0.04 \Big(\dfrac{1200\,\mathrm{AU}}{\overline{z}}\Big)^{5.1} + 0.25 \Big(\dfrac{\overline{z}}{1200\,\mathrm{AU}}\Big)^{2.65}}} \Big(\frac{d}{1\,\mathrm{m}}\Big)^{\frac{3}{2}} \Big(\frac{1.3\,\mathrm{pc}}{z_0}\Big) \Big(\frac{\overline{z}}{1200\,\mathrm{AU}}\Big)^{1.7} \sqrt{\frac{t}{1\,\mathrm{s}}}. \tag{26}$$

We also estimated the SNR of the convolved image for an exoplanet at $z_0 = 30$ pc and the telescope at heliocentric distance of $\overline{z} = 650$ AU. This quantity is easy to compute from (9) and (19) in the following form:

$$\mathrm{SNR}_{\mathtt{C}}(\rho_0) = \frac{1.68\,\mu(\rho_0)}{\sqrt{1 + 0.79 \Big(\dfrac{650\,\mathrm{AU}}{\overline{z}}\Big)^{5.1} + 0.05 \Big(\dfrac{\overline{z}}{650\,\mathrm{AU}}\Big)^{2.65}}} \Big(\frac{d}{1\,\mathrm{m}}\Big)^{\frac{3}{2}} \Big(\frac{30\,\mathrm{pc}}{z_0}\Big) \Big(\frac{\overline{z}}{650\,\mathrm{AU}}\Big)^{1.7} \sqrt{\frac{t}{1\,\mathrm{s}}}. \tag{27}$$

B. SNR of the deconvolved image

To estimate the impact of deconvolution on the signal-to-noise ratio, consistent with [19] and [5] we model the exoplanet as source with a uniform brightness and represent the image as a collection of N pixels. We denote the post-deconvolution signal-to-noise ratio as $\mathrm{SNR}_{\mathtt{R}}$.

In [5] we estimated the deconvolution penalty as

$$\frac{\mathrm{SNR}_{\mathtt{R}}}{\mathrm{SNR}_{\mathtt{C}}} = \frac{\dfrac{1}{N} \displaystyle\sum_{i=1}^{N} \sum_{j=1}^{N} C_{ij}^{-1}}{\Big(\dfrac{1}{N} \displaystyle\sum_{i=1}^{N} \sum_{j=1}^{N} (C_{ij}^{-1})^2\Big)^{\frac{1}{2}}}, \tag{28}$$

where C_{ij} is the convolution matrix and N is the total number of image pixels. To estimate the inverse of the convolution matrix, we approximated it in the form

$$C_{ij} \sim \tilde{C}_{ij} = \frac{4}{\pi\alpha d}(\mu\delta_{ij} + \nu U_{ij}), \tag{29}$$

where δ_{ij} is the Kronecker-delta, U_{ij} is the everywhere-one matrix, $\nu \ll 1$ and $\mu = 1 - \nu$.

We can estimate ν using the averaged SGL PSF and replacing summations over large N with integrals:

$$\nu = \frac{1}{A} \iint\limits_{x,y=-\sqrt{N}d/2}^{\sqrt{N}d/2} dxdy \frac{d}{4\sqrt{x^2+y^2}} = \frac{4}{\pi} \frac{\ln(\sqrt{2}+1)}{\sqrt{N}}, \tag{30}$$

where the light collecting area is given by $A \sim N\pi\frac{1}{4}d^2$, consistent with our PSF estimates assuming a telescope with a circular aperture used to traverse the image plane and sample image pixels.

Using this approximation allowed us to explicitly calculate $\tilde{C}_{ij}^{-1}$ and thus estimate the deconvolution penalty for large N, $\mu \sim 1$, as

$$\frac{\mathrm{SNR}_\mathtt{R}}{\mathrm{SNR}_\mathtt{C}} = \frac{\dfrac{1}{N}\displaystyle\sum_{i=1}^{N}\sum_{j=1}^{N}\tilde{C}_{ij}^{-1}}{\Big(\dfrac{1}{N}\displaystyle\sum_{i=1}^{N}\sum_{j=1}^{N}(\tilde{C}_{ij}^{-1})^2\Big)^{\frac{1}{2}}} = \frac{\mu}{\nu N} \sim \frac{0.891}{\sqrt{N}}. \tag{31}$$

This result describes image deconvolution using adjacent pixels.

When pixels are not adjacent, however, ν is scaled by d/D where we denote the pixel spacing by D. Thus we obtain the following estimate for the deconvolution penalty:

$$\frac{\mathrm{SNR}_\mathtt{R}}{\mathrm{SNR}_\mathtt{C}} \sim 0.891\frac{D}{d\sqrt{N}}. \tag{32}$$

Numerical simulations using a variety of images, resolutions, and pre-deconvolution Gaussian noise consistently confirm that the penalty is indeed proportional to $1/\sqrt{N}$ with a numerical coefficient of $\sim 0.891D/d$.

C. Estimating the required integration time

Given a target $\mathrm{SNR}_\mathtt{R}$ after deconvolution, we can estimate the pre-deconvolution value of $\mathrm{SNR}_\mathtt{C}$ and consequently, the required integration time by solving for t in Eqs. (23), (26) or (27).

For a target $\mathrm{SNR}_\mathrm{R} = 10$, using $D = d$, $N = 10^6$, and omitting the numerical prefactor in (32), we obtain, for an exoplanet at 1.3 pc and with the telescope at 1200 AU, $\mathrm{SNR}_\mathrm{C} = 10000$ and a total integration time of $Nt = 1.03 \times 10^{11}$ s $= 3.26 \times 10^3$ years, which is prohibitive. (NB: This value is higher than the estimate in [19]; we attribute this difference to an ambiguity concerning the factor f used in that study.)

However, it is important to note that the image of an exo-Earth at 1.3 pc, projected to an image plane at 1200 AU from the Sun, is almost 60 km wide. Therefore, in case a megapixel image is sought, individual image plane pixels will not be adjacent: they will be $D = 60$ meters apart. Consequently, the integration time penalty for a $d = 1$ will scale by a factor of $(d/D)^2 = 1/3600$, which is much less than one year.

To obtain the best estimate, normalized to our nominal mission baseline with a telescope at 650 AU and an exo-Earth up to 100 light years from the Earth, we use (27). The total integration time required to obtain an image of N pixels is

$$\begin{aligned} T(\rho_0) = Nt(\rho_0) &= 0.354\,\mu(\rho_0)N\mathrm{SNR}_\mathtt{C}^2\Big(\frac{1\ \mathrm{m}}{d}\Big)^3\Big(\frac{z_0}{30\ \mathrm{pc}}\Big)^2\Big(\frac{650\ \mathrm{AU}}{\overline{z}}\Big)^{3.4}\Big(1+0.79\Big(\frac{650\ \mathrm{AU}}{\overline{z}}\Big)^{5.1}+0.05\Big(\frac{\overline{z}}{650\ \mathrm{AU}}\Big)^{2.65}\Big) \\ &= 0.446\,\mu(\rho_0)N^2\mathrm{SNR}_\mathtt{R}^2\Big(\frac{1\ \mathrm{m}}{d}\Big)\Big(\frac{1\ \mathrm{m}}{D}\Big)^2\Big(\frac{z_0}{30\ \mathrm{pc}}\Big)^2\Big(\frac{650\ \mathrm{AU}}{\overline{z}}\Big)^{3.4}\Big(1+0.79\Big(\frac{650\ \mathrm{AU}}{\overline{z}}\Big)^{5.1}+0.05\Big(\frac{\overline{z}}{650\ \mathrm{AU}}\Big)^{2.65}\Big). \end{aligned} \tag{33}$$

Using $d = 1$ m, $D = 60$ m, $z_0 = 1.3$ pc, $\overline{z} = 1200$ AU, $\rho_0 = 0$, for $\mathrm{SNR}_\mathtt{R} = 10$ and $N = 10^6$ we obtain $T \sim 43$ days. For comparison, at the nominal mission limit of $z_0 = 30$ pc, $\overline{z} = 650$ AU, a good quality image with $\mathrm{SNR}_\mathtt{R} = 3$, using $N = 128 \times 128$ image pixels, is obtainable in 1.75 years.

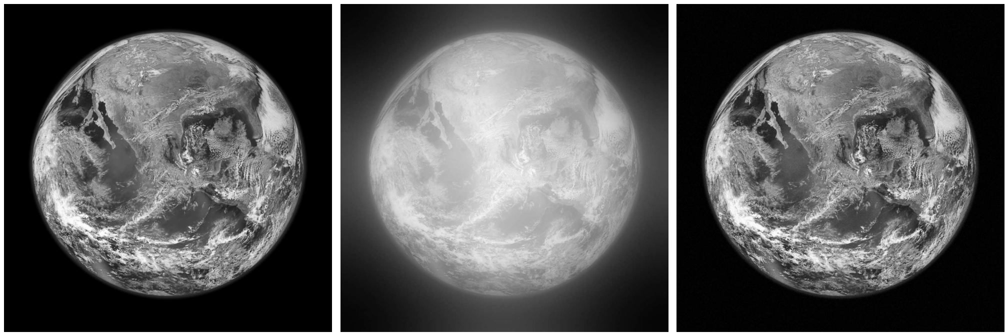

FIG. 5: Simulated monochromatic imaging of an exo-Earth at $z_0 = 1.3$ pc from $\overline{z} = 1200$ AU at $N = 1024 \times 1024$ pixel resolution using the SGL. Left: the original image. Middle: the image convolved with the SGL PSF, with noise added at $\mathrm{SNR_C} = 187$, consistent with a total integration time of ∼47 days. Right: the result of deconvolution, yielding an image with $\mathrm{SNR_R} = 11.4$.

These results are confirmed by numerical simulation. An example, shown in Fig. 5, uses an image of the Earth, convolved with the SGL PSF, corrupted by Gaussian noise at $\mathrm{SNR_C} = 187$, and deconvolved using model parameters $z_0 = 1.3$ pc, $\overline{z} = 1200$ AU. The numerically obtained $\mathrm{SNR_R} = 11.4$ is consistent with the fact that instead of a uniformly illuminated disk, an actual planetary image was used with variable levels of brightness.

This example also highlights why pixel spacing has such a substantial effect on the deconvolution penalty and the resulting integration time. As the middle image in Fig. 5 shows, when pixels are spaced widely apart, the blur due to the SGL's spherical aberration is substantially reduced. Even in the convolved image, detailed features of the Earth's topography are recognizable. This would not be the case if pixels were adjacent. Consequently, when pixels are far apart, deconvolution introduces a relatively modest penalty, very significantly reducing the required integration time to obtain a high-resolution image of a target exoplanet.

V. DISCUSSION AND CONCLUSIONS

The SGL is characterized by the geometric properties of the Einstein ring that appears around the Sun, when viewed from a vantage point in the SGL's focal region. The diameter of this Einstein ring ($> 2R_\odot$) and its light collecting area ($> 2\pi R_\odot d$) determine its angular resolution and light amplification capabilities, respectively, both of which are many orders of magnitude beyond the capabilities offered by conventional telescopes or even proposed optical interferometric configurations.

For this reason, the SGL is being considered as a means to obtain detailed images of Earth-like exoplanets in other solar systems, at resolutions that cannot be obtained by any other existing or foreseeable technical solution. A major challenge is that the SGL is not a perfect lens. It is characterized by substantial negative spherical aberration. A further complication is that any light from a distant source appears as an Einstein ring near the solar disk, on the background of the very bright solar corona.

The SGL's PSF is known. This makes it possible, in principle, to reconstruct sharp, detailed images of the observational target. The unwanted background from the solar corona can be measured independently and removed. Inevitably, due to the quantized nature of light, stochastic shot noise with approximately Gaussian characteristics remains. Reducing this noise can only be accomplished by increasing the amount of light collected, using either larger instruments or longer integration times.

We estimated the impact of mission parameters on the resulting integration time. We found that, as expected, the integration time is proportional to the square of the total number of pixels that are being imaged. We also found, however, that the integration time is reduced when pixels are not adjacent, at a rate proportional to the inverse square of the pixel spacing.

Consequently, using a fictitious Earth-like planet at the Proxima Centauri system at $z_0 = 1.3$ pc from the Earth, we found that a total cumulative integration time of less than 2 months is sufficient to obtain a high quality, megapixel scale deconvolved image of that planet. Furthermore, even for a planet at 30 pc from the Earth, good quality deconvolution at intermediate resolutions is possible using integration times that are comfortably consistent with a realistic space mission.

A mission that begins its imaging campaign at 650 AU would thus benefit from the increasing SNR as it progresses to larger heliocentric distances [6]. This would allow such a mission to gradually improve its resolution, while keeping integration times sufficiently short to study temporally varying effects, such a diurnal rotation.

There are other challenges. In this study, we modeled the solar gravitational field as a monopole field, not yet accounting for deviations in the form of the field's quadrupole and higher moments. We also have not yet accounted for the aforementioned temporal effects, including planetary motion, rotation, and varying illumination. This work is on-going (e.g., [26–29] for multipolar contributions and [30] for properly capturing the dynamics), along with work on establishing a technically feasible mission design and architecture. Results will be published elsewhere when available.

Acknowledgments

This work in part was performed at the Jet Propulsion Laboratory, California Institute of Technology, under a contract with the National Aeronautics and Space Administration. The authors are grateful to Karl R. Stapelfeldt and Phil A. Willems of JPL for motivation and helpful discussions. VTT acknowledges the generous support of Plamen Vasilev and other Patreon patrons.

[1] W. A. Traub and B. R. Oppenheimer, *Direct Imaging of Exoplanets* ("Exoplanets", University of Arizona Press, Tucson, AZ, 2010), pp. 111–156.
[2] J. T. Wright and B. S. Gaudi, *Exoplanet Detection Methods* (Springer, Dordrecht, Netherlands, 2013), p. 489.
[3] R. Angel, in *Earths: DARWIN/TPF and the Search for Extrasolar Terrestrial Planets*, edited by M. Fridlund, T. Henning, and H. Lacoste (2003), vol. 539 of *ESA Special Publication*, pp. 221–230.
[4] S. G. Turyshev and V. T. Toth, Phys. Rev. D **96**, 024008 (2017), arXiv:1704.06824 [gr-qc].
[5] S. G. Turyshev and V. T. Toth, Phys. Rev. D **102**, 024038 (2020), arXiv:2002.06492 [astro-ph.IM].
[6] S. G. Turyshev, M. Shao, V. T. Toth, L. D. Friedman, L. Alkalai, D. Mawet, J. Shen, M. R. Swain, H. Zhou, H. Helvajian, et al., *Direct multipixel imaging and spectroscopy of an exoplanet with a solar gravity lens mission, NIAC Final Report on Phase II Award* (2020), arXiv:2002.11871 [astro-ph.IM].
[7] S. Seager, *Exoplanet Atmospheres: Physical Processes* (Princeton University Press, Princeton, NJ, 2010).
[8] S. G. Turyshev and V. T. Toth, Phys. Rev. D **100**, 084018 (2019), arXiv:1908.01948 [gr-qc].
[9] S. G. Turyshev and V. T. Toth, Phys. Rev. D **101**, 044025 (2020), arXiv:1909.03116 [gr-qc].
[10] S. G. Turyshev and V. T. Toth, Phys. Rev. D **101**, 044048 (2020), arXiv:1911.03260 [gr-qc].
[11] V. T. Toth and S. G. Turyshev, Phys. Rev. D (2020), arXiv:2012.05477 [gr-qc].
[12] M. Shao, H. Zhou, and S. G. Turyshev, *Design for the SGL Extended Source Coronagraph* (2017), unpublished.
[13] H. Zhou, *SGL Coronagraph Simulation* (2018), unpublished, URL `https://www.kiss.caltech.edu/workshops/solar/solar.html`.
[14] M. Shao, *Multipixel (megapixel) image of an exoplanet* (2018), unpublished, URL `https://www.kiss.caltech.edu/workshops/solar/solar.html`.
[15] S. G. Turyshev et al., *Direct Multipixel Imaging and Spectroscopy of an Exoplanet with a Solar Gravity Lens Mission.* The Final Report for the NASA's Innovative Advanced Concepts (NIAC) Phase I proposal (2018), arXiv:1802.08421.
[16] S. G. Turyshev and V. T. Toth, Phys. Rev. D **99**, 024044 (2019), arXiv:1810.06627 [gr-qc].
[17] S. G. Turyshev and V. T. Toth, Eur. Phys. J. Plus **134**, 63 (2019), arXiv:1811.06515 [gr-qc].
[18] G. A. Landis, *Mission to the gravitational focus of the sun: A critical analysis* (2016), arXiv:1604.06351 [astro-ph.EP].
[19] P. A. Willems, Acta Astronautica **152**, 408 (2018).
[20] S. G. Turyshev, Phys. Rev. D **95**, 084041 (2017), arXiv:1703.05783 [gr-qc].
[21] M. Abramowitz and I. A. Stegun, *Handbook of Mathematical Functions: with Formulas, Graphs, and Mathematical Tables.* (Dover Publications, New York; revised edition, 1965).
[22] B. Lyot, Zeitschrift für Astrophysik **5**, 73 (1932).
[23] L. J. November and S. Koutchmy, Astrophys. J. **466**, 512 (1996).
[24] S. Baumbach, Astronomische Nachrichten **263**, 121 (1937).
[25] L. Golub and J. M. Pasachoff, *The Solar Corona* (2-nd edition. Cambridge University Press, Cambridge, England, 2009).
[26] S. G. Turyshev and V. T. Toth, Phys. Rev. D **103**, 064076 (2021), arXiv:2102.03891 [gr-qc].
[27] S. G. Turyshev and V. T. Toth, Phys. Rev. D **104**, 024019 (2021), arXiv:2103.06955 [gr-qc].
[28] S. G. Turyshev and V. T. Toth, Phys. Rev. D **104**, 044032 (2021), arXiv:2104.08442 [gr-qc].
[29] S. G. Turyshev and V. T. Toth, Phys. Rev. D **104**, 124033 (2021), arXiv:2105.07295 [gr-qc].
[30] S. G. Turyshev and V. T. Toth, Phys. Rev. D **105**, 044012 (2022), arXiv:2112.03019 [gr-qc].